DOE-ET-53088-143 IFSR #143

EFFECTS OF A RADIAL ELECTRIC FIELD ON TOKAMAK EDGE TURBULENCE

T. Chiueh, P.W. Terry, P.H. Diamond, and J.E. Sedlak
Institute for Fusion Studies
The University of Texas at Austin
Austin, Texas 78712

March 1985

Effects of a Radial Electric Field on Tokamak Edge Turbulence

T. Chiueh, P.W. Terry, P.H. Diamond, and J.E. Sedlak
Institute for Fusion Studies
The University of Texas at Austin
Austin, Texas 78712

Abstract

Turbulence associated with sheared radial electric fields such as those arising in tokamak edge plasmas is investigated analytically. Two driving mechanisms are considered: in the region of maximum vorticity (maximum electric field shear), the electric field is the dominant driving mechanism. Away from the maximum, turbulence is driven by the density gradient. In the latter case, previous work is extended to include the effects of the electric field on the spatial scales of density correlation in the frequency-Doppler-shifted density-gradient-driven turbulence. For radial electric field driven turbulence, the effects of magnetic shear on linear instability and on fully developed turbulence are examined. In the case of weak magnetic shear, saturation occurs through an enstrophy cascade process which couples regions of driving and dissipation in wavenumber space. For stronger magnetic shear, such that the resistive layer is comparable to the radial electric field scale length, saturation occurs through nonlinear broadening of the mode structure, which pushes enstrophy into the region of dissipation. Estimates of mode widths, fluctuation levels and scalings are obtained for both mechanisms. Comparison is made with the results of fluctuation measurements in the TEXT tokamak.

I. Introduction

Recent measurements of turbulence in the edge region of tokamaks indicate the existence of a time-independent radial electric field.[1,2] This field is large (50 volt/cm), has a very steep gradient ($L_E \approx 1$ cm) and reverses sign near the limiter. Its scale length is $L_E/\rho_i \approx 10$. Fluctuation measurements in the region of maximum gradient show an isotropic spectrum with widths in frequency and wavenumber which exceed by a factor of two the anisotropic spectra measured away from the maximum (Fig. 1).[1] These measurements are corroborated by flow visualizations, assembled from probe array data which suggest the presence of vortex-like motion in this region.[3]

The radial variation of the electric field implies rotation in the ion diamagnetic direction outside the limiter and rotation in the electron direction further in (radially). It is thus possible, on the basis of an electric field dependent Doppler shift in frequency, to reconcile theories which predict phase velocities in the electron direction[4,5] with measurements made at the extreme edge which indicate phase velocities in the ion direction.[6,7] However it also becomes necessary to determine the effects of a radial electric field on turbulence in the edge region. The fact that broadened spectra are observed both away from and near a strong vorticity maximum and have a character which changes noticibly near the maximum suggest that both "standard" density or temperature-gradient-driven turbulence and electric-field-gradient-driven turbulence play a role in determining edge turbulence spectra. Furthermore, nonambipolar transport processes have recently been proposed[8,9] as relevant to understanding the separatrix region of diverted H-mode discharges. The shear flow

stability properties of plasmas, which support the electric fields that result, is therefore also important for understanding H-mode profiles and confinement.

In this paper we explore the effects of a radial electric field on edge turbulence models. A sheared radial electric field is included in a two-point theory of density-gradient-driven turbulence developed previously. It is found that the correlation decay rate due to (velocity) shear induced relative drift is greater than that due to the ambient turbulence. The extent to which this enhanced decay affects the scale size is calculated quantitatively using the theory of two-point correlation[5]. On the basis of these results, we conclude that the electric field shear alone is strong enough to determine the radial density correlation length at the maximum (velocity) shear region. Thus, the strength of the shear suggests that its role as a free energy source for instabiltiy should also be examined.

For turbulence driven by the gradient of the radial electric field, we study the shear flow (Rayleigh) instability and consider additional (stabilizing) effect of magnetic shear. The linear growth rate and eigenfunction structure are obtained using the reduced MHD equations in the electrostatic limit, and an approximate radial electric field profile. In the limit of vanishing magnetic shear damping, this instability reduces to the familiar Rayleigh instability, where flow shear relaxes by an interchange of vortex tubes around a vorticity maximum, in which case restoring forces vanish. Moreover, as the linear mode structure is broad and has approximately the same length scales in the radial and poloidal directions, an isotropic spectrum is expected.

Two possible nonlinear saturation mechanisms are proposed, and the saturation level corresponding to each is estimated. The strength of the magnetic shear damping relative to that of the destabilizing source determines which mechanism is operative. When magnetic shear is weak, saturation of unstable modes relies on an enstrophy cascade which transfers mode energy from unstable modes to high k stable modes. When magnetic shear is moderate or strong, fewer modes are destabilized. For those remaining unstable, saturation results from nonlinear mode broadening (Fig. 6) which effectively transfers energy from the source (vorticity gradient) to the sink. For parameters consistent with the TEXT tokamak, magnetic shear damping is moderately strong in the edge, and the latter mechanism is expected to determine saturation.

For a model shear-flow profile, $V_E(x) = V_0 \tanh \frac{x}{L_E}$, the saturation level of the root-mean-square potential fluctuations is

$$\frac{e\Phi_{rms}}{T_e} \sim \frac{1}{4\sqrt{3}(k_0 L_E)} \left(\frac{V_0}{\rho_s C_s k_{MIN}}\right) ,$$

in the case where saturation arises from a cascade process. This result is easily recognized as the familiar mixing-length fluctuation level. At such levels, the coupling to the higher k stable modes is equal to input from the gradient source. For saturation due to nonlinear broadening of mode structure, the rms potential fluctuation level at saturation is

$$\frac{e\Phi_{rms}}{T_e} \sim \left(\frac{1}{k_0 L_E R^2}\right)^{15/16} \left(\frac{V_0 L_E}{C_s \rho_s}\right) ,$$

where k_0 and k_{MIN} are the average and minimum wavenumbers respectively, C_s is sound speed, ρ_s is the ion gyroradius with electron temperature, and

$$R^2 = \left(\frac{4\pi V_A^2}{c^2}\right) \cdot \left(\frac{L_E^3}{\eta V_0 L_s^2}\right) ,$$

characterizing the strength of magnetic shear, V_A is Alfvén speed, η is the resistivity and L_s is the magnetic shear length. At such levels, convection to dissipation at finite $\underset{\sim}{k}\cdot\underset{\sim}{B}_0$ equals input from the gradient source. We find that when $R = 2.6(k_{MIN}L_E)^{1/2}$, transition from one regime to the other occurs.

We also estimate the density and magnetic field fluctuation levels. In an incompressible fluid, density fluctuations arise from the convection of fluid elements along the density gradient by the fluctuating velocity field; magnetic field fluctuations result from the coupling of the electric and magnetic fields via Ohm's law. When the cascade process is responsible for saturation, the saturated density and magnetic field fluctuations are

$$\frac{\delta n_{rms}}{n_0} \sim \frac{L_E}{L_n}$$

$$\frac{\tilde{B}_{rms}}{B_0} \sim \frac{\pi}{\sqrt{3}} \left(\frac{L_E V_0}{\eta L_s k_{MIN} c^2}\right) .$$

When the mechanism of nonlinearly mode-structures broadening dominates saturation, they are

$$\frac{\delta n_{rms}}{n_0} \sim \frac{L_E}{L_n} \left(\frac{1}{k_0 L_E R^2}\right)^{5/16}$$

$$\frac{\tilde{B}_{rms}}{B_0} \sim \left(\frac{V^2_0 L_s}{V^2_A L_E}\right) \left(\frac{1}{k_0 L_E R^2}\right)^{9/16} ,$$

where L_n is the density scale length.

For the parameters in the tokamak edge of TEXT, $T_e \cong 20eV$, $n_0 \cong 2\times10^{12}cm^{-3}$, $Z_{eff} \cong 3\sim4$ $B_0 \cong 0.7\times10^4$ Gauss, $V_0 \cong 3\times10^5 cm/sec$ $L_E \cong 0.5cm$, $L_n \cong 1.5cm$, $L_s \cong 200\sim400cm$, we estimate $R\cong2$ for $L_s \cong 300cm$, and the root-mean-square fluctuation levels at saturations are

$$\frac{e\Phi_{rms}}{T_e} \sim 0.42 \quad , \quad \frac{\delta n_{rms}}{n_0} \sim 0.35 \quad , \quad \text{and}$$

$$\frac{\tilde{B}_{rms}}{B_0} \sim 5\times10^{-5} .$$

The values for $e\Phi/T_e$ and $\frac{\delta n}{n_0}$ are consistent with those measured.

The remainder of this paper is organized as follows: In Sec. II, we extend the previous study of density-gradient driven turbulence to incorporate the inhomogeneous radial electric field and examine the

consequences. In Sec. III, we make a preliminary linear analysis of the fluctuations driven by the radial electric field gradient. This analysis reveals a key point for nonlinear saturation, discussed later. In Sec. IV, we outline the renormalization scheme, and propose two competing saturation mechanisms characterized by the strength of magnetic shear. Subsequently, various of relevant quantities are estimated in Sec. V and compared with those obtained from experiments. Finally, conclusions are discussed in Sec. VI.

II. Effect of an Electric Field on the Density Fluctuation Correlation Function

We first study density gradient-driven turbulence and consider the fluid equations for dissipative drift waves in a torus. The electrons are adiabatic and isothermal, $[\omega\nu_{ei} < v_{Te}^2/(Rq)^2]$ and are collisional on the transit time scale; i.e., $\nu_{ei} > \omega_{Te} = v_{Te}/(Rq)$. The linear properties of these equations are discussed in Refs. 5 and 11.

With the inclusion of a radial electric field, a time-independent E×B drift is added. The convection of density by this drift results in a Doppler-shifted frequency. Thus the equation for the non-adiabatic part of the electron density H is

$$-i(\omega-\omega_E)H_{\underset{\omega}{n}} - \frac{v_{Te}^2}{\nu_{ei}(Rq)^2}\frac{\partial^2}{\partial\eta^2}H_{\underset{\omega}{n}} + N_{\underset{\omega}{n}} = \frac{i|e|}{T_e}(\omega-\omega_E-\omega_{*e})\varphi_{\underset{\omega}{n}} \qquad (1)$$

where n is the toroidal mode number, η is the coordinate along the magnetic field direction and $N_{\underset{\omega}{n}}$ is the E×B nonlinearity, in the ballooning representation. The symbol ω_{*e} refers to the diamagnetic

drift frequency, $\omega_{*e} = (CT_e/eB)k_\vartheta/L_n$, where $k_\vartheta = nq/r$. The electric field induced Doppler shift is represented by ω_E, where $\omega_E = -\frac{C}{B_0} E_r k_\vartheta = V_E k_\vartheta$. For edge plasma parameters typical of Text[1], Pretext[7] and the Caltech tokamak[6], ω_E (10^6 rad/sec) can exceed ω_{*e} (10^5 rad/sec) by an order of magnitude or more except in the close vicinity of the electric field null point. This implies that measured phase velocities of edge fluctuations are primarily determined by the electric field, with a shift due to ω_{*e}. Hence, the phase velocities can be in the opposite direction of the electron drift.

To determine the effect of the radial electric field on density correlations in the turbulent flow, we study the two-point density correlation $\langle H(1)H(2)\rangle$. The equation for two-point density correlation is readily derived from the one-point equation. Standard renormalization procedures may be applied to the nonlinearity to obtain an equation with diffusion in the relative variables, $(y_-,n_-,r_1) = \frac{1}{2}(y_1-y_2,\eta_1-\eta_2,r_1-r_2)$:

$$\left[\frac{\partial}{\partial t} - \frac{C}{B_0} r_- \frac{E_0}{L_E}\frac{\partial}{\partial y_-} - \frac{v_{Te}^2}{(Rq)^2\nu_{ei}}\frac{\partial^2}{\partial \eta_-^2} - D_-(y_-,\eta_-,r_-)\cdot\frac{\partial^2}{\partial y_-^2}\right]\langle H(1)H(2)\rangle$$

$$= S = \sum_{\substack{k'\\ \omega'}} \frac{i|e|}{T_e}\left(e^{ik'y_-}\right)(\omega'-\omega_E'-\omega_{*e}')\langle H(1)\phi(2)\rangle_{k'\omega'} \qquad (2)$$

where $D_-(y_-,\eta_-,r_-)$ is the renormalized turbulent diffusion coefficient for the predominant (y_-) diffusion. According to Eq. (2), the two-point density correlation is governed by the competition of the driving source on the right-hand side with the decay processes of relative diffusion and drift on the left-hand side. The driving source

is fed by the density gradient and is homogeneous in the relative coordinate. It is the inhomogeneities associated with the decay which determine the spatial dependence of the correlation function. The decay processes are 1) the relative drift between fluid elements at different points on the drift velocity profile $V_E(r) = \frac{C}{B_0} E_r(r) \approx \frac{CE_0}{B_0} \frac{r}{L_E}$, 2) the relative parallel diffusion due to collisional viscosity and 3) the inhomogeneous relative diffusion due to the turbulent E×B mixing. Note that while the E×B diffusion vanishes as the relative separation goes to zero (a consequence of correlation in the scattering field at short separation), the parallel collisional diffusion does not. Because of this property the density correlation peaks at small scale, but is finite at zero relative separation.

For small relative separation the turbulent diffusion is given approximately as

$$D_- = D\left(k_0^2 y_-^2 + \eta_-^2/\Delta\eta^2 + k_0^2 \hat{s}^2 r_-^2\right) . \tag{3}$$

where $$\varphi(r) = \sum_m e^{imy} \sum_n e^{i(n-mq)\eta} \int d\eta\ \varphi(\eta) ,$$

and $$D = \frac{c^2}{B_0^2} \sum_{k'} k_{\vartheta}'^2 \hat{s}^2 \mathrm{Re}\left[\omega' - \omega_E' - \frac{v_{Te}^2 \frac{\partial^2}{\partial\eta^2}}{im_e \nu_{ei}}\right]^{-1} \sum_m (2\pi m)^2 \langle \varphi(\eta+2\pi m)^2 \rangle_{k'} .$$

The quantities k_0^{-2}, $(Rq\Delta\eta)^2$ and $(k_0\hat{s})^{-2}$ are the poloidal $\left(k = \frac{nq}{r}\right)$, parallel and radial scales on which the relative diffusion begins to decrease from its asymptotic value D. The poloidal scale corresponds to a typical wavenumber in the spectrum. The parallel scale is determined

by the toroidicity-induced eigenmode structure. The relation $\Delta r = (k\hat{s})^{-1}$ is a consequence of ballooning representation.

The spatial dependence of the steady state solution of Eq. (2) is obtained by the inversion of the operator on the left-hand side of Eq. (2) which yields $\tau_{c1}(y_-,\eta_-,r_-)$, the two-point correlation time. The correlation time is calculated by taking moments of the L.H.S. of Eq. (2), which yields differential equations governing the evolution of neighboring fluid element positions.[5,12] For the operator in Eq. (2) the correlation time is

$$\tau_{c1}(y_-,\eta_-,r_-) = (k_0^2 D)^{-1} \ln\{[k_0^2(y_-^2 + \eta_-^2/\Delta\eta^2 k_0^2 + \frac{R_e^{-1}}{k_0^2} + (\hat{s}^2 + \frac{1}{2}\frac{c^2E_0^2}{B_0^2L_E^2}\frac{1}{k_0^4D^2})r_-^2)]^{-1}\} \quad (4)$$

where $R_e = Dk_0^2(Rq)^2\Delta\eta^2\nu_{ei}/v_{Te}^2$ is the Reynolds number and parameterizes the relative strengths of the linear (parallel collisional viscosity) and nonlinear (E×B diffusion) processes. For Reynolds numbers exceeding order unity, Eq. (4) exhibits logarithmic peaking inside the correlation scale. The correlation scales are determined by the coefficients of the relative coordinates. The scale of radial correlation is thus

$$\Delta r = (\hat{s}^2 + \frac{1}{2}\frac{c^2E_0^2}{B_0^2L_E^2}\frac{1}{k_0^4D^2})^{-1/2} k_0^{-1}$$

$$= \left(\hat{s}^2 + \left(\frac{\tau_c}{\tau_E}\right)^2\right)^{-1/2} k_0^{-1} , \qquad (5)$$

where $\tau_c = \frac{1}{k_0^2 D}$, the correlation time, and $\tau_E = \frac{\sqrt{2} B_0 L_E}{C E_0}$, the dynamical time scale of the poloidal flow. For parameters consistent with the edge plasmas already referred to,[1,6,7] τ_E is comparable to τ_c and the correlation scale determined from Eq. (5) is of the order of 1 cm. For $k_0^{-1} \sim 10\rho_s$ this is qualitative agreement with the radial correlation scale measured in the TEXT[1] and Caltech tokamak.[10] However, at the region of maximum flow shear,

$$\tau_c/\tau_E > \hat{s} \approx 1 .$$

This observation that τ_E is the shortest dynamically relevant time scale suggests that effects of the electric field gradient on edge turbulence may be more involved than a simple Doppler shift. Thus, in the next section, we shall thus examine the electric field gradient as a driving mechanism for turbulence.

III. Radial-Electric-Field-Driven Turbulence: Basic Analysis

We now examine electric-field driven fluctuations. In a magnetized plasma, the radial electric field, $-\nabla_r \Phi(r)$, causes a poloidal drift $V_E = (C/B_0^2)\, \underline{B}_0 \times \nabla_r \Phi$. Since this radial electric field has spatial dependence, the resulting plasma flow is a source of free energy and can potentially drive instabilities. In the case of strong toroidal magnetic fields, plasma motion is quasi-two-dimensional; the electric potential Φ can be looked upon as the flow stream function,

and $\nabla_\perp^2\Phi$ as the vorticity. Suitable equations for description of the vorticity evolution in the tokamak edge are the reduced MHD equations,[15]

$$\rho \frac{d}{dt} \nabla_\perp^2\varphi = B_0\nabla_\parallel J_\parallel + \nabla_\perp A_\parallel \times \hat{b} \cdot \nabla_\perp J_\parallel \tag{6}$$

$$\frac{d}{dt} A_\parallel = \frac{B_0}{c^2} \nabla_\parallel \varphi + \eta J_\parallel \ , \tag{7}$$

where $\varphi \equiv \Phi c^2/B_0$, $\hat{b} = \underline{B}_0^{(r)}/B_0^{(r)}$, and $A_\parallel$ and $J_\parallel$ are the vector potential and current along the field line, respectively.

Here, the dynamical time and length scales are approximately determined by the shear flow, i.e., $|\frac{d}{dt}| \sim \frac{V_0}{L_E}$, and $|\nabla_\perp| \sim \frac{1}{L_E}$. When comparing the electromagnetic piece, $\frac{dA_\parallel}{dt}$, with the current piece, $\eta J_\parallel (= \frac{\eta c^2}{4\pi} \nabla_\perp^2 A_\parallel)$, of the parallel Ohm's law, Eq. (7), we find $\eta c^2/4\pi V_0 L_E >> 1$, and the electromagnetic piece, $\frac{dA_\parallel}{dt}$, can be dropped. Hence, using the electrostatic limit of Ohm's law, reduced MHD yields the vorticity equation,

$$\rho \frac{d}{dt} \nabla_\perp^2 \varphi = \frac{B_0^2}{\eta c^2} \nabla^2{}_\parallel \varphi \ . \tag{8}$$

In the limit of vanishing magnetic shear ($\nabla_\parallel$=0), Eq. (8) gives

$$\frac{d}{dt} \nabla_\perp^2 \varphi = 0 \ ,$$

which is a statement of conservation of vorticity. It is well-established that a necessary condition for instability in this

equation is the existence of a vorticity maximum at the point of inflection of the equilibrium flow $V_E(r)$.[13,14] In view of this criterion, the profiles of Ritz et al. clearly point to the possibility of shear flow driven turbulence in the tokamak edge.

Shear flow instability is associated with the interchange of vortex tubes at the vorticity maximum, where the restoring force vanishes. Any localized perturbed motion around this point cannot be stopped, thus instability arises.

When magnetic shear is considered, free energy provided by the vorticity gradient can be dissipated by the resistive dissipation. Thus instability can be effectively suppressed unless the vorticity maximum coincides with the location of the magnetic resonance surface. There, the dissipation associated with $\nabla_\parallel J_\parallel$ is minimized, and instability can be locally excited for the longest wavelength modes. To simplify the analysis, we will use slab geometry, with x and y representing the radial and poloidal directions respectively. We then Fourier transform Eq. (8) with respect to y and the parallel variable and obtain

$$\left[\frac{\partial}{\partial t} + ikV_E(x)\right]\nabla_\perp^2\varphi_k - ik\frac{d^2V_E}{dx^2}\varphi_k - k^2R^2(x-x_0)^2\varphi_k$$

$$= i\sum_{k'}\left[k'\nabla_\perp^2\varphi_{k'}\frac{d\varphi_{k''}}{dx} - k'\varphi_{k'}\frac{d}{dx}\nabla_\perp^2\varphi_{k''}\right], \qquad (9)$$

where $k \equiv k_y$, velocity, length and time variables are normalized to the characteristic shear flow velocity V_0, the width of shear flow L_E and their ratio L_E/V_0 respectively, and φ is normalized to $L_E V_0$. In

addition, we have used $k_{\parallel}^2 = k^2(x-x_0)^2/L_s^2$ to account for the magnetic shear, hence $R^2 = 4\pi V_A^2 L_E^2/\eta V_0 C^2 L_s^2$, where V_A is the Alfvén speed. Note that the magnitude of the sink term relative to that of the source term is kR^2. This defines a length $L_E/(kR^2)^{1/2}$ for the dissipation-free region where the source is much stronger than the sink.

Linearly unstable modes can be locally excited within the dissipation-free region if the energy source (with a width of the shear layer L_E) decouple from the linear dissipation. Stability is crucially dependent on the degree of overlap between the energy source and dissipation region. Long wavelength modes have a larger dissipation-free region, and thus are easier to excite. In the limit of large R, the unstable wavenumber k must be be sufficiently small in order for the energy source to overcome dissipation. Consequently, kR^2 for the unstable modes will approach a constant of order unity, as R becomes much larger than unity. Further increase in R can force the wavenumber k to be smaller than the system allows, k_{MIN}, and yields stability.

In order to discuss stability and describe turbulence properties, it is necessary to specify profiles for $V_E(x)$. $V_E(x)$ is measured in TEXT and appears to be essentially linear in the region of interest. Outside the linear region, the velocity profile is flat. For simplicity, we model this observed profile with a hyperbolic tangent,

$$V_E(x) = V_0 \tanh \frac{x}{L_E} .$$

We solve the linearized eigenvalue problem of Eq. (9) numerically to determine the frequency. The eigenfunctions, which are purely growing

and excited around the central region, are shown in Fig. 2. It is noted that the length scale of a linear mode in the dissipation-free region is different from that of the dissipation region. The former can be estimated by comparing the linear convective term with the gradient source and is approximately,

$$\Delta_i^L \approx L_E \ ; \tag{10}$$

the latter by balancing the inertia term with the sink and is approximately,

$$\Delta_0^L \approx \frac{L_E}{(2kR^2)^{1/4}} \ . \tag{11}$$

The relevance of these two length scales will be discussed in the next section.

In Fig. 3, we show the growth rate γ_k versus the wavenumber k for various values of R. In the above, we have chosen $x_0 = 0$, i.e., the vorticity maximum is centered at the $\underline{k}\cdot\underline{B}_0 = 0$ surface. As R increasing, unstable modes are confined to those of increasingly longer wavelengths, and the maximum growth rates decrease. When the vorticity maximum is not centered at the $\underline{k}\cdot\underline{B}_0 = 0$ surface, $x_0 \neq 0$, the modes become more stable, as shown in Fig. 4, because greater overlap occurs between the energy source and the dissipation region (Fig. 5). This damping is a sort of dissipative line-tying. In the more unstable $x_0 = 0$ case, we find that kR^2 for the most unstable modes asymptotically approaches 0.5 from below, as R becomes very large.

For TEXT parameters, R is of order unity, hence magnetic shear, though significant, is not sufficient to suppress the hydrodynamic shear-flow instability. To study turbulence caused by this instability, a nonlinear analysis is then necessary.

IV. Nonlinear Analysis and Saturation Mechanisms

In this section, we investigate possible saturation mechanisms. In the present case, two processes compete to drain wave energy from the unstable modes. Both rely on parallel dissipation and turbulent diffusion; however, the role of turbulent diffusion in each of these two processes is distinct. In the first process, turbulent diffusion nonlinearly couples different modes, permitting energy flow in k space which reaches the high-k energy sink. In the second process, turbulent diffusion broadens the mode structures, allowing energy to reach regions in x space with strong dissipation (Fig. 6).

To renormalize Eq. (9), a standard iterative method is used to approximate its convective nonlinearity. The nonlinear vorticity evolution equation can be expressed as (with $x_0 = 0$),

$$[-i\omega+ikV_E(x)]\nabla_\perp^2\varphi_{k,\omega} + \frac{1}{2}\{\frac{d}{dx}\sum_{\substack{k'\\ \omega'}}[(ik')\varphi_{k',\omega'}\nabla_\perp^2\varphi_{k'',\omega''} - (ik')\varphi_{k'',\omega''}\nabla_\perp^2\varphi_{k',\omega'}]$$

$$-ik\sum_{\substack{k'\\ \omega'}}[\frac{d\varphi_{k',\omega'}}{dx}\nabla_\perp^2\varphi_{k'',\omega''}-\varphi_{k'',\omega''}\frac{d\nabla_\perp^2\varphi_{k',\omega'}}{dx}]\} = ik\frac{d^2V_E}{dx^2}\varphi_{k,\omega}-k^2R^2X^2\varphi_{k,\omega} \quad . \quad (12)$$

This equation can be renormalized by substituting $\varphi_{k'',\omega''}$ and $\nabla_\perp^2\varphi_{k'',\omega''}$ for $\varphi^{(2)}_{k'',\omega''}$ and $\nabla_\perp^2\varphi^{(2)}_{k'',\omega''}$ respectively, where the latter quantities are driven by the direct beating of a test (k,ω) mode and background

(k',ω') modes (detailed derivation of local and nonlocal renormalized terms, $D_{k,\omega}$ and $C_{k,\omega}$, respectively, is shown in Appendix (A)).

In the present analysis, we shall neglect the nonlocal $C_{k,\omega}$ and retain only the more familiar $D_{k,\omega}$, local operators of diffusion type, to model the effects of random convection by the turbulent velocity field. It is evident, from Eq. (A-4), that $D_{k,\omega}$ is composed of the diffusion of both vorticity $\nabla_\perp^2\varphi_{k,\omega}$ and field $\varphi_{k,\omega}$ in the x and y directions. That is,

$$D_{k,\omega} = [\frac{d}{dx} D_x \frac{d}{dx} - k^2 D_y]\nabla_\perp^2\varphi_{k,\omega} - [\frac{d}{dx} d_x \frac{d}{dx} - k^2 d_y]\varphi_{k,\omega} . \qquad (13)$$

The linear convection together with diffusion of vorticity describe the perturbed orbit of a vorticity element, while the diffusion of the field describes modifications of the equilibrium profiles. As pointed out by Dupree, these two effects cancel in the total energy (not energy per mode) evolution equation.[16] In the present case of spatially inhomogeneous profiles, they combine to form a term of a total derivative with respect to x, representing the divergence of energy flux. Hence, these two groups of terms in $D_{k,\omega}$ account for the nonlinear spatial rearrangement of the kinetic energy.

In the region where $|\varphi_{k,\omega}|^2$ is large, we have $|\frac{d^2}{dx^2}| >> k^2$. Hence we retain only $\frac{d}{dx} D_x \frac{d}{dx} \nabla_\perp^2\varphi_{k,\omega}$ to represent the locally renormalized nonlinearity. The nonlinear evolution equation for vorticity can thus be approximated by

$$[\frac{\partial}{\partial t} + ikV_E - D \frac{d^2}{dx^2}]\nabla_\perp^2\varphi_k = [ik \frac{d^2V_E}{dx^2} + k^2R^2X^2)\varphi_k , \qquad (14)$$

and that of the vorticity spectrum by

$$\int dx\{\frac{\partial}{\partial t}\,|\nabla_\perp^2\varphi_k|^2 + 2D|\frac{d}{dx}\,\nabla_\perp^2\varphi_k|^2 - 2(\sum_{k'}\,|\frac{d}{dx}\,\nabla_\perp^2\varphi_{k'}|^2)D_k\}$$

$$= 2\int dx\{-k\,\frac{d^2V_E}{dx^2}\,\mathrm{Im}\langle\varphi_k\nabla_\perp^2\varphi_k^*\rangle + k^2R^2X^2\mathrm{Re}\langle\varphi_k\nabla_\perp^2\varphi_k^*\rangle\}\ , \qquad (15)$$

where the third term on the left of Eq. (15) is the nonlinear incoherent source. Together with the diffusion term, these two nonlinear terms are responsible for enstrophy cascade. Here, D is given explicitly by

$$D = \sum_k D_k \qquad (16)$$

and

$$D_k \cong \frac{k^2|\varphi_k|^2}{(\omega+ikV_E(x) + D\,\frac{d^2}{dx^2})}\ . \qquad (17)$$

In the remainder of this section, we separately present the details of the two nonlinear saturation processes previously mentioned. As the parameter R effectively determines which of the processes dominates, we consider the limits $R \ll 1$ and $R \cong O(1)$ respectively.

(A) $R \ll 1$

In this regime, the linear sink is very weak for a broad range of low-k modes. The dissipation region is spatially remote from the region, where unstable modes are located, because the width of the

dissipation-free region scales as $L_E\,(kR^2)^{-1/2}$. Thus, the linearly unstable modes do not sense the magnetic shear. Only those modes with sufficiently large wavenumbers experience appreciable linear dissipation. As a result, the only significant way available for the removal of wave energy from unstable modes is by a nonlinear coupling between low-k and high-k modes. This coupling allows an energy flow in k space toward the high-k dissipation range exactly as in the conventional picture of cascading. In the renormalized theory this nonlinear coupling is represented by turbulent diffusion which removes energy from the low-k linearly unstable modes.

Ignoring magnetic shear, we have an equation for low-k linearly unstable modes,

$$\left[-i\omega+ikV_E-D\,\frac{d^2}{dx^2}\right]\nabla_\perp^2\varphi_{k,\omega} = ik\,\frac{d^2V_E}{dx^2}\,\varphi_{k,\omega} \qquad (18)$$

This is the Orr-Sommerfeld equation, and the stability boundary has been tabulated. For the hyperbolic-tangent flow profile, the longest wavelength modes are always unstable in spite of a large value of D. Hence the complete stabilization of all modes must rely on the existence of a lower bound of k, which may be imposed by finite system size or by other effects not contained in this model. For small kL_E, the Reynolds number, $R_e = \frac{V_0 L_E}{D}$, satisfies

$$R_e \cong 4\sqrt{3}\;kL_E \qquad (19)$$

at the stability boundary. Thus the diffusion coefficient is approximately

$$D \cong \frac{V_0 L_E}{4\sqrt{3}\, k_{MIN} L_E} \tag{20}$$

at saturation, where k_{MIN} is the lower bound of the range of wavenumbers.

(B) $R \sim O(1)$

In this regime, magnetic shear very effectively governs the stability of low-k modes. The stability is determined by the competition of vortex interchange and magnetic shear. Spatially, the dissipation region lies in close proximity to the free energy source (Fig. 2), thus stability is crucially dependent on the degree to which these two regions overlap. Nonlinearly, it is more effective for the linear sink to couple to the source, through real space by spatial broadening, than through k space as in the previous case. Here, turbulent diffusion creates a mode structure which extends into the dissipative region (Fig. 6), through which energy flows to parallel resistive sink. Thus, turbulent diffusion nonlinearly couples source and sink.

Let Δ_i and Δ_0 be the characteristic lengths of the nonlinearly broadened mode in the inner (source) and outer (sink) regions, respectively. To determine them at saturation, one can use Eq. (14) and balance the diffusion of vorticity with the source in the inner region, and the sink in the outer region, respectively. That is,

$$\frac{D}{\Delta_i^4}\,\varphi_k \cong |k\langle\frac{d^2V_E}{dx^2}\rangle|\varphi_k \cong k\,\frac{\bar{V}_0}{L_E^2}\,\varphi_k$$

$$\frac{D}{\Delta_0^4}\,\varphi_k \cong k^2R^2\Delta_0^2\varphi_k \ .$$

Here, we have ignored the convection in the presence of diffusion of vorticity. In addition, we have approximated the averaged d^2V_E/dx^2 in the inner region with a value V_0/L_E^2. Hence it follows that

$$\Delta_i \cong \left(\frac{D}{k}\right)^{1/4} \tag{21}$$

$$\Delta_0 \cong \left(\frac{D}{k^2R^2}\right)^{1/6} \ . \tag{22}$$

To determine D, we need to use Eq. (15), the vorticity spectrum equation. At steady state,

$$\int dx\,\frac{\partial}{\partial t}\,|\nabla_\perp^2\varphi_k|^2 = 0 \ ,$$

and the remaining pieces of Eq. (15) are the nonlinear enstrophy coupling terms on the left-hand side and the competition between driving and dissipation terms on the right. In this regime, nonlinear cascade of enstrophy is less effective and can be neglected. Saturation occurs when the source balances the linear sink. Substituting $\nabla_\perp^2\varphi_k$ from Eq. (14) in Eq. (15), one obtains

$$0 = \int \frac{dx}{k^2 V_E^2 + (D\,\frac{d^2}{dx^2})^2} \left[k^2 \left(\frac{d^2 V_E}{dx^2}\right)^2 \left(D\,\frac{d^2}{dx^2}\right) + k^4 R^4 X^4 \left(D\,\frac{d^2}{dx^2}\right)\right] |\varphi_k|^2 = 0 \ ,$$

where $D\,d^2/dx^2$ operates only on φ_k. Since φ_k is a localized function in x (Fig. 2), peaked at the inner region and evanescent in the dissipation region, $d^2/dx^2 \cong -1/\Delta_i^2$ for the source term and $d^2/dx^2 \cong 1/\Delta_0^2$ for the sink term. As a result, it follows that

$$\frac{1}{4}\,\Delta_i^2 \cong k^2 R^4 \Delta_0^7 \ , \tag{23}$$

where the convection term in the denominator has been ignored, and $|d^2 V_E/dx^2| \sim V_0/L_E^2$ has been used. In addition, the integral $\int dx$ has been evaluated with the values L_E (because of the localization of the source, $d^2 V_E/dx^2$) in the inner regions, and Δ_0 in the outer region.

D, Δ_i and Δ_0 can now be straightforwardly determined using Eqs. (21), (22) and (23). Thus,

$$\Delta_i = \left(\frac{1}{kR^2}\right)^{5/16} L_E \tag{24}$$

$$\Delta_0 = \left(\frac{1}{kR^2}\right)^{3/8} L_E \tag{25}$$

$$D = \frac{V_0 L_E}{(kR^2)^{1/4} R^2} \ . \tag{26}$$

Comparing the nonlinear scale lengths (Eqs. (24) and (25)) with the

linear ones (Eqs. (10) and (11)), we find that the nonlinear scale lengths are broadened ($kR^2 \leq 1$).

V. Estimate of Fluctuation Levels at Saturation

Having obtained the vorticity diffusion coefficients D for both saturation mechanisms, we are now able to estimate several relevant quantities for comparison with experiments. The quantities include the root-mean-square potential, density and magnetic field fluctuations. These quantities will be estimated separately, for each saturation mechanism.

At steady-state, the vorticity diffusion coefficient D, arising from the random convection of velocity field, can be expressed as

$$D \cong \sum_k \frac{k^2|\varphi_k|^2}{ikV_E(x) - D\frac{d^2}{dx^2}} \cong \frac{1}{\left(\frac{D}{\Delta_i^2}\right)} \sum_k k^2|\varphi_k|^2 \cong \frac{k_0^2<\varphi^2>\Delta_i^2}{D} , \tag{27}$$

hence the rms potential fluctuation level is approximately

$$\frac{e\Phi_{rms}}{T_e} \cong \frac{D}{\rho_s C_s}\frac{1}{k_0\Delta_i} , \tag{28}$$

where C_s is the ion sound speed and ρ_s is the ion gyroradius with electron temperature. In the above expression (and hereafater), the original unit of Φ as the electric potential has been (and will be) retained.

The magnetic field fluctuation is related to the current fluctuation $J_{\parallel}$ by Ampere's law,

$$[\nabla \times \tilde{\underline{B}}]_{\parallel} = \frac{4\pi}{C} J_{\parallel} ,$$

and the current fluctuation couples to the electric potential fluctuation through the electrostatic Ohm's law, $-\nabla_{\parallel}\Phi = \eta J_{\parallel}$. Hence the rms magnetic field is approximately

$$\frac{\tilde{B}_{rms}}{B_0} \cong \left(\frac{4\pi k_0 \Delta_i^2}{\eta L_s \omega_{c_i}}\right)\left(\frac{C_s^2}{C^2}\right)\left(\frac{e\Phi_{rms}}{T_e}\right) . \tag{29}$$

To estimate the density fluctuation, it is noted that in this model of electric-field-driven turbulence the density gradient has been ignored, and so has the density fluctuation. Obviously, density gradient effects and density fluctuations significantly complicate this simple model, making analysis difficult. However, because the density gradient is smaller than that of the equilibrium flow in the region of interest, the effects of density gradient and density fluctuations on the evolution of vorticity are probably small in this case. We can estimate the saturation level of density fluctuations by consideration of a model, where density evolves by convection of the velocity field as a passive scalar. That is,

$$\frac{dn}{dt} = 0 . \tag{30}$$

Fourier-transforming Eq. (30) in the y-direction and renormalizing its nonlinear terms, we have

$$\left[\frac{\partial}{\partial t} + ikV_E(x) - D\frac{d^2}{dx^2}\right]\delta n_k = ik\Phi_k\left(\frac{C}{B_0}\right)\cdot\frac{dn_0}{dx} \quad . \tag{31}$$

At saturation, we again neglect the convection of density fluctuations by the equilibrium flow in comparison with the diffusion term. Balancing the latter with the density fluctuation caused by fluctuating velocity fields randomly oscillating across the density gradient, we then obtain the rms density fluctuation level

$$\frac{\delta n}{n_0} \cong \frac{\Delta_i}{L_n} \quad . \tag{32}$$

Substituting Δ_i, Δ_0 and D from Eqs. (10), (11) and (20) into Eqs. (28), (29) and (32), we obtain the fluctuation levels at saturation due to the nonlinear cascade process,

$$\frac{e\Phi_{rms}}{T_e} \cong \frac{1}{4\sqrt{3}k_0L_E}\left(\frac{V_0}{\rho_s C_s k_{MIN}}\right) \tag{33}$$

$$\frac{\tilde{B}_{rms}}{B_0} \cong \frac{\pi}{\sqrt{3}}\left(\frac{L_E V_0}{\eta L_s k_{MIN} C^2}\right) \tag{34}$$

$$\frac{\delta n_{rms}}{n_0} \cong \frac{L_E}{L_n} \quad . \tag{35}$$

Substituting Δ_i, Δ_0 and D from Eqs. (24), (25) and (26) into Eq. (28), (29) and (32), we obtain the fluctuation levels due to the nonlinearly broadened-mode-structure mechanism,

$$\frac{e\Phi_{rms}}{T_e} \cong \left(\frac{1}{k_0 L_E R^2}\right)^{15/16} \left(\frac{V_0 L_E}{\rho_s C_s}\right) \tag{36}$$

$$\cong \frac{e}{T_e} \cdot \left(\frac{\eta L_s^2 M_i n_0}{k_0 L_E}\right)^{15/16} \left(\frac{C}{B_0}\right)^{7/8} V_0^{31/16} L_E^{-29/16} \tag{36a}$$

$$\frac{\tilde{B}_{rms}}{B_0} \cong \left(\frac{1}{k_0 L_E R^2}\right)^{9/16} \left(\frac{V_0^2 L_s}{V_A^2 L_E}\right) \tag{37}$$

$$\cong \left(\frac{\eta c^2}{4\pi k_0 L_E}\right)^{9/16} V_0^{41/16} L_s^{17/8} V_A^{-25/8} L_E^{-13/4} \tag{37a}$$

and

$$\frac{\delta n_{rms}}{n_0} \cong \frac{L_E}{L_n} \left(\frac{1}{k_0 L_E R^2}\right)^{5/16} \tag{38}$$

$$\cong \frac{1}{L_n} \left(\frac{\eta V_0 L_s^2 C^2}{4\pi k_0 L_E V_A^2}\right)^{5/16} L_E^{1/16} \tag{38a}$$

Notice that for R much greater than unity, $k_0 L_E$ is forced to be small, and asymptotically approaches the value 1/2R from below. Hence the expressions Eqs. (36), (37) and (38) should be used to determine scalings. For R not too much greater than unity, $k_0 L_E$ is relatively insensitive to the value of R and the expressions Eqs. (36a), (37a) and (38a) should be used for scaling laws. In the large R limit, we also

notice that $\Delta_i \rightarrow L_E$, provided that k_{MIN} is small enough so that there is a range of small k satisfying this asymptotic limit.

As R decreases from unity the results predicted by the broadened-mode-structure processed do not approach those of the cascade processes. The reason is obvious, for they correspond to two different, competing physical processes. The critical value of R at which transition from one process to the other occurs can be estimated in the following way. Intuitively one expects that the saturation levels for the cascade process should be greater than those of the broadened-mode-structure processes, since the latter involves coupling to linear damping that can directly draw energy from the source and inhibit large fluctuation amplitudes. In this case, the critical value of R occurs when the diffusion coefficients of both processes are equal. That is, $R_{crit} \cong 2.6(k_{MIN}L_E)^{1/2}$.

For parameters consistent with those of the TEXT tokamak in the edge, $R \cong 2$ and $R_{crit} \cong 0.4$, hence the broadened-mode-structure mechanism prevails. The estimated saturation levels are

$$\frac{e\varphi_{rms}}{T_e} \cong 0.42$$

$$\frac{\delta n_{rms}}{n_0} \cong 0.35 \ .$$

$$\frac{\tilde{B}_{rms}}{B_0} \cong 5\times10^{-5}$$

These values of fluctuation levels do not dramatically differ from those of density-gradient-driven turbulence. This is because the

correlation time scales of both types of turbulence (Eq. 5) are comparable for the parameters of TEXT experiments, hence comparable spectral amplitudes are expected.

VI. Summary and Conclusion

An analytical theory is developed to describe tokamak edge turbulence associated with the presence of a sheared radial electric field. Turbulence in this region can be driven by the density gradient and radial-electric-field gradient. Near the region where the maximum velocity shear of the equilibrium $E_0 \times B_0$ poloidal flow is located, the flow shear alone is strong enough to drive fluctuation. In the linear phase, energy provided by sources is partially dissipated by the sink, i.e., electron collisionality along field lines; the remainder is used to excite fluctuations. If the coupling of the sink to the source is made very effective through nonlinear modifications of the basic modes, fluctuations can be stabilized. For steady-state turbulence, energy provided by the source is then totally absorbed by the sink.

In this paper, we have separately studied turbulence driven by the density gradient in the presence of radial electric field and that by the electric field gradient. For the former, effects of radial electric field do not drastically change the basic characteristics of turbulence, but simply modify them. Results of this study on the modifications of density-gradient-driven turbulence in the presence of the radial electric field can be summarized as follows:

1) The phase velocities of fluctuations are locally Doppler-shifted by the mass flow of $E_0 \times B_0$ convection (Eq. (1)). This is indeed what has been observed at the region away from the vorticity maximum in the edge of TEXT tokamak.

2) Inhomogeneity of the radial electric field leads to an additional decay mechanism (Eq. (2)) for density correlation arising from shear in the poloidal velocity field. As a result, the gradient of the radial electric field reduces the radial correlation length (Eq. (5)), and thus enhances spectral anisotropy. At the region of maximum electric field gradient, the effects of flow shear are too large to be treated perturbatively.

Near the region of the equilibrium vorticity maximum, the driving force of flow shear alone is strong enough to yield hydrodynamic instability. The density gradient in this region is ignored. The principal results for electric-field-gradient-driven turbulence are:

1) For relatively strong collisionality, $R(= \frac{4\pi V_A^2 L_E^3}{\eta V_0 L_s^2 C^2})$ not much larger than unity, as typically occurs in the tokamak edge, the mode structures are spatially broad: the length scales in the poloidal and radial directions are comparable. This indicates that the fluctuation spectrum of electric-field-gradient-driven turbulence is nearly isotropic.

2) Linear growth rates have been obtained. They indicate that instabilities are dependent sensitively on the degree of overlap between the regions of the energy source (vorticity gradient) and sink (parallel resistive dissipation). Furthermore, it is found that the long wavelength linear modes can be unstable due to a lack of sufficient overlap.

3) Nonlinearity is approximated by turbulent diffusion of vorticity for linearly unstable modes. Two types of nonlinear processes are simultaneously present governing the evolution of turbulence. They are the nonlinear cascade and nonlinear broadening of mode structure. The former process produces coupling between modes of different wavenumbers, whereby wave energy of unstable modes can be extracted by the short-wavelength, linearly stable modes. The latter process radially broadens mode structures, which permits the sink to directly extract energy from the source and stabilize linear instabilities. A dimensionless quantity R, characterizing the strength of magnetic shear , determines which of these two mechanisms is dominant. When $R \ll 1$, the region of magnetic shear damping is separated from that of energy input. The latter mechanism is not effective and the nonlinear cascade then provides saturation. When $R \cong O(1)$, the location of the sink is not far from that of the source and slight broadening of mode width can effectively yield saturation.

4) Diffusion coefficients and the rms potential, magnetic field and density fluctuations at saturation have separately been estimated for each regime. For paramaters of the TEXT tokamak in the edge, we have estimated R≅2, hence turbulence is governed by the mechanism of nonlinear broadening of mode structure. The saturation levels of potential, density and magnetic field fluctuations estimated by this theory are consistent with those observed in experiments.

It is interesting to note that, in the limit of small R, the long wavelength modes cannot be saturated by finite turbulent diffusion, and hence the complete saturation necessitates a lower bound for wavenumbers, i.e., k_{MIN}, which is usually determined by system sizes. The inability of turbulent diffusion to saturate the low-k modes actually lies in the fact that there is no characteristic length in the region away from the shear layer, thus the spatial derivative d/dx scales as k^{-1}. Hence the rate of decorrelation $\left(|D \frac{d^2}{dx^2}| \cong k^2 D\right)$ can only offset the growth rate ($\gamma_k \propto k$) if $D \propto k^{-1}$ (thus $D \to \infty$ as $k \to 0$). By contrast, saturation mechanism in the strong magnetic shear limit introduces another length scale $L_E/(2kR^2)^{1/2}$ in addition to the length scale L_E of the source. This extra degree of freedom allows turbulent diffusion to regulate the mode width so as to defeat the linear growth rate to a considerable extent ($D \propto k^{-1/4}$).

Saturation mechanisms of this type represent a departure from the conventional the mixing length theory. It is instructive to contrast this theory with mixing-length theory and speculate as to its generality. In this model, instead of using the width and e-folding

time of linear modes as the correlation length and decorrelation time, the latter quantities have been self-consistently determined. Moreover, as the sink (parallel dissipation) is located at a certain distance from the source, an additional length scale is introduced. This extra degree of freedom allows turbulent diffusion to adjust and yields a completely different correlation length and time from those of linear theory.[17]

This type of nonlinear mechanism may have a wide range of generality, particularly for turbulence in the vicinity of single-helicity magnetic resonance surface, $\underline{k}\cdot\underline{B}_0 = 0$. For the case where magnetic field fluctuations are as important as electric field fluctuations (see Sec. III), i.e., $\eta c^2/4\pi V_0 L_E \lesssim 1$, shear-flow-driven magnetic reconnection may occur. We expect that a similar, but more involved, analysis should apply.

In summary, this paper has explored possible mechanisms responsible for the turbulence observed in the vicinity of the equilibrium vorticity maximum in the tokamak edge. The idea of the nonlinearly broadened mode structures, developed here and elsewhere, is seen to play an important role in the characterization of steady-state turbulence and should prove to be useful in other contexts.

Acknowledgments

The authors would like to thank C.P. Ritz, R.D. Bengtson, S.J. Levinson, B.A. Carreras, and C.M. Surko for useful discussions related to this work. This work was supported by the U.S. Department of Energy contract no. DE-FG05-80ET-53088.

Appendix (A)

Here we give the detailed derivation of renormalization for Eq. (12). The nonlinear terms can be renormalized by substituting $\varphi_{k'',\omega''}$ and $\nabla_\perp^2\varphi_{k'',\omega''}$ for $\varphi^{(2)}_{k'',\omega''}$ and $\nabla_\perp^2\varphi^{(2)}_{k'',\omega''}$ respectively, where the latter quantities are driven by the direct beating of a test (k,ω) mode and background (k',ω') modes. These driven modes satisfy

$$\nabla_\perp^2\varphi^{(2)}_{k'',\omega''} \cong \int dx' \left[\frac{-i\nabla_\perp^2 G_{k'',\omega''}(x,x')}{\omega''-k''V_E(x')}\right]\left[ik'\nabla_\perp^2\varphi^*_{k',\omega'}\frac{d\varphi_{k,\omega}}{dx'} - ik'\varphi^*_{k',\omega'}\right.$$

$$\left.\cdot\frac{d}{dx'}\nabla_\perp^2\varphi_{k,\omega} - ik\nabla_\perp^2\varphi_{k,\omega}\frac{d\varphi^*_{k',\omega'}}{dx'} + ik\varphi_{k,\omega}\frac{d}{dx'}\nabla_\perp^2\varphi^*_{k',\omega'}\right] \qquad (A-1)$$

$$\varphi^{(2)}_{k'',\omega''} \cong \int dx' \left[\frac{-iG_{k'',\omega''}(x,x')}{\omega''-k''V_E(x')}\right]\left[ik'\nabla_\perp^2\varphi^*_{k',\omega'}\frac{d\varphi_{k,\omega}}{dx'} - ik'\varphi^*_{k',\omega'}\right.$$

$$\left.\cdot\frac{d}{dx'}\nabla_\perp^2\varphi_{k,\omega} - ik\nabla_\perp^2\varphi_{k,\omega}\frac{d\varphi^*_{k',\omega'}}{dx'} + ik\varphi_{k,\omega}\frac{d}{dx'}\nabla_\perp^2\varphi^*_{k',\omega'}\right] , \qquad (A-2)$$

where $G_{k'',\omega''}(x,x')$ is a linear propagator satisfying

$$\nabla_\perp^2 G_{k'',\omega''}(x,x') = \frac{-1}{\omega''-k''V_E(x)}\left[k''\frac{d^2V_E}{dx^2} - ik''^2R^2X^2\right]G_{k'',\omega''}(x,x')+\delta(x-x')$$

$$\equiv L_{k'',\omega''}(x)\ G_{k'',\omega''}(x,x') + \delta(x-x') \ . \qquad (A-3)$$

Together with Eqs. (A-1), (A-2) and (A-3), nonlinear terms become

$$[NL]_{k,\omega}$$

$$\cong \sum_{\substack{k',\\ \omega'}} \Big\{\Big(\frac{d}{dx}\Big\{\Big(\frac{i}{\omega''-k''V_E}\Big)(k')^2\Big[\langle\varphi_{k',\omega'}\nabla_\perp^2\varphi^*_{k',\omega'}\rangle \frac{d\varphi_{k,\omega}}{dx} - \langle|\varphi_{k',\omega'}|^2\rangle \frac{d}{dx}\nabla_\perp^2\varphi_{k,\omega}\Big]\Big\}$$

$$-k^2\Big\{\Big(\frac{i}{\omega''-k''V_E}\Big)\Big[\Big\langle\frac{d\varphi_{k',\omega'}}{dx}\frac{d}{dx}\nabla_\perp^2\varphi^*_{k',\omega'}\Big\rangle\varphi_{k,\omega} - \Big\langle\Big|\frac{d\varphi_{k',\omega'}}{dx}\Big|^2\Big\rangle\nabla_\perp^2\varphi_{k,\omega}\Big]\Big\}\Big\}$$

$$+ \sum_{\substack{k',\\ \omega'}} \int dx'\Big(\frac{i}{\omega''-k''V_E(x')}\Big)\Big\{(k')^2\frac{d}{dx}\Big\{\Big[L_{k'',\omega''}(x)G_{k'',\omega''}(x,x')\langle\varphi_{k',\omega'}(x)\nabla_\perp^2\varphi^*_{k',\omega'}(x')\rangle$$

$$- G_{k'',\omega''}(x,x')\cdot\langle\nabla_\perp^2\varphi_{k',\omega'}(x)\nabla_\perp^2\varphi^*_{k',\omega'}(x')\rangle\Big]\frac{d\varphi_{k,\omega}}{dx'}$$

$$-\Big[L_{k'',\omega''}(x)G_{k'',\omega''}(x,x')\langle\varphi_{k',\omega'}(x)\varphi^*_{k',\omega'}(x')\rangle$$

$$- G_{k'',\omega''}(x,x')\cdot\langle\nabla_\perp^2\varphi_{k',\omega'}(x)\varphi^*_{k',\omega'}(x')\rangle\Big]\frac{d\nabla_\perp^2\varphi_{k,\omega}}{dx'}\Big\}$$

$$- k^2\Big\{\Big[L_{k'',\omega''}(x)G_{k'',\omega''}(x,x')\Big\langle\frac{d\varphi_{k',\omega'}}{dx}\frac{d\nabla_\perp^2\varphi^*_{k',\omega'}}{dx'}\Big\rangle$$

$$- G_{k'',\omega''}(x,x')\Big\langle\frac{d\nabla_\perp^2\varphi_{k',\omega'}}{dx}\frac{d\nabla_\perp^2\varphi^*_{k',\omega'}}{dx'}\Big\rangle\Big]\varphi_{k,\omega}(x')$$

$$- \Big[L_{k'',\omega''}(x)G_{k'',\omega''}(x,x')\Big\langle\frac{d\varphi_{k',\omega'}}{dx}\frac{d\varphi^*_{k',\omega'}}{dx'}\Big\rangle$$

$$- G_{k'',\omega''}(x,x')\Big\langle\frac{d\nabla_\perp^2\varphi_{k',\omega'}}{dx}\frac{d\varphi^*_{k',\omega'}}{dx'}\Big\rangle\Big]\nabla_\perp^2\varphi_{k,\omega}(x')\Big\}\Big\} \equiv D_{k,\omega} + C_{k,\omega} \quad . \qquad (A-4)$$

Terms in the first spectral sum, $D_{k,\omega}$, arise from the local response ($\delta(x-\bar{x})$ of Eq. (A-3)) of the driven vorticity $\nabla_\perp^2\varphi^{(2)}_{k'',\omega''}$. Terms in the second spectral sum $C_{k,\omega}$, are due to both the nonlocal response ($L_{k'',\omega''}G_{k'',\omega''}$ of Eq. (A-3)) of the driven vorticity $\nabla_\perp^2\varphi^{(2)}_{k'',\omega''}$ and driven field $\varphi^{(2)}_{k'',\omega''}$.

References

1. C.P. Ritz, R.D. Bengtson, S.J. Levinson and E.J. Powers, Phys. Fluids 27, 2956 (1984).

2. S.J. Zweben, private communication.

3. S.J. Zweben, accepted by and to appear in Phys. Fluids.

4. A. Hasegawa and M. Wakatani, Phys. Rev. Lett. 48, 1828 (1982).

5. P.W. Terry and P.H. Diamond, Institute for Fusion Studies Report #114, (1984), accepted by and to appear in Phys. Fluids.

6. S.J. Zweben and R.W. Gould, Nucl. Fusion 23, 1625 (1983).

7. S.J. Levinson, J.M. Beall, E.J. Powers and R.D. Bengtson, Nucl. Fusion 24, 527 (1984).

8. F.L. Hinton, et al., Proc. 10th Int. Conf. on Plasma Phys. and Contr. Nucl. Fusion., London (1984).

9. F. Wagner, et al., Phys. Rev. Lett. 53, 1453 (1984).

10. S.J. Zweben and R.W. Gould, Bull. Amer. Phys. Soc. 28, 1204 (1983).

11. L. Chen, M.S. Chance and C.Z. Cheng, Nucl. Fusion 22, 293 (1983).

12. T.H. Dupree, Phys. Fluids 15, 334 (1972).

13. C.C. Lin, The Theory of Hydrodynamic Stability, Cambridge University Press, 1955.

14. P.G. Drazin and L.N. Howard, Adv. Appl. Mech. 9, 1 (1966).

15. H.R. Strauss, Phys. Fluids 20, 1354 (1977).

16. T.H. Dupree and D.J. Tetreault, Phys. Fluids 21, 425 (1978).

17. L. Garcia, P.H. Diamond, B.A. Carreras, and J.D. Callen, IFS Report #146, 1984.

Figure Captions

Fig. 1: Radial profile of vorticity and fluctuation spectra measured by Ritz, et al., (C.P. Ritz, et al., Phys. Fluids 27, 2956) (1984)). The standard deviations of the measured spectra, $\sigma(k_r)$ and $\sigma(k_\vartheta)$, indicate the change of turbulence characteristics, from an isotropic spectrum at high velocity shear to anisotropic spectra at low velocity shear. (Figure used with permission)

Fig. 2: Linearly unstable eigenfunction, and locations of the (shear flow) driving source and (resistive) sink. The driving source is centered at the minimum of the magnetic shear of R=2, thus avoids dissipation. The localized eigenfunction φ_k of k=0.08 is excited. The source vorticity is indicated by the dotted line; the sink is in the shaded region; and the eigenfunction $|\varphi_k|^2$ is indicated by the solid line.

Fig. 3: Growth rate γ_k vs. wavenumber k, with $x_0 = 0$, i.e., the driving source centered at the minimum of magnetic shear. Modes of intermediate values of k have the greatest growth rates. As magnetic shear R increases, γ_k is reduced.

Fig. 4: Growth rate γ_k vs. wavenumber k, with $x_0 = 1$, i.e., the driving source having a large portion overlapped with the sink. When compared with Fig. 3, the growth rates are significantly reduced.

Fig. 5: Linearly <u>stable</u> eigenfunction, and locations of the (shear flow) driving source and (resistive) sink. The driving source is not centered at the minimum of the magnetic shear of R=2, hence leads to a large region of overlap. The eigenfunction φ_k of k=0.08 is therefore stabilized. The source vorticity is indicated by the dotted line; the sink is in the shaded region; and the eigenfunction $|\varphi_k|^2$ is indicated by the solid line.

Fig. 6: A comparison of linear and nonlinear eigenfunctions. The nonlinear mode $|\varphi_k^{NL}|^2$ is broader and extends into the dissipation region. Here, R=2 and k=0.02. The source vorticity is indicated by the dotted line; the sink is in the shaded region; the linear eigenfunction $|\varphi_k|^2$ is indicated by the solid line; and the nonlinear eigenfunction is indicated by the dash line.

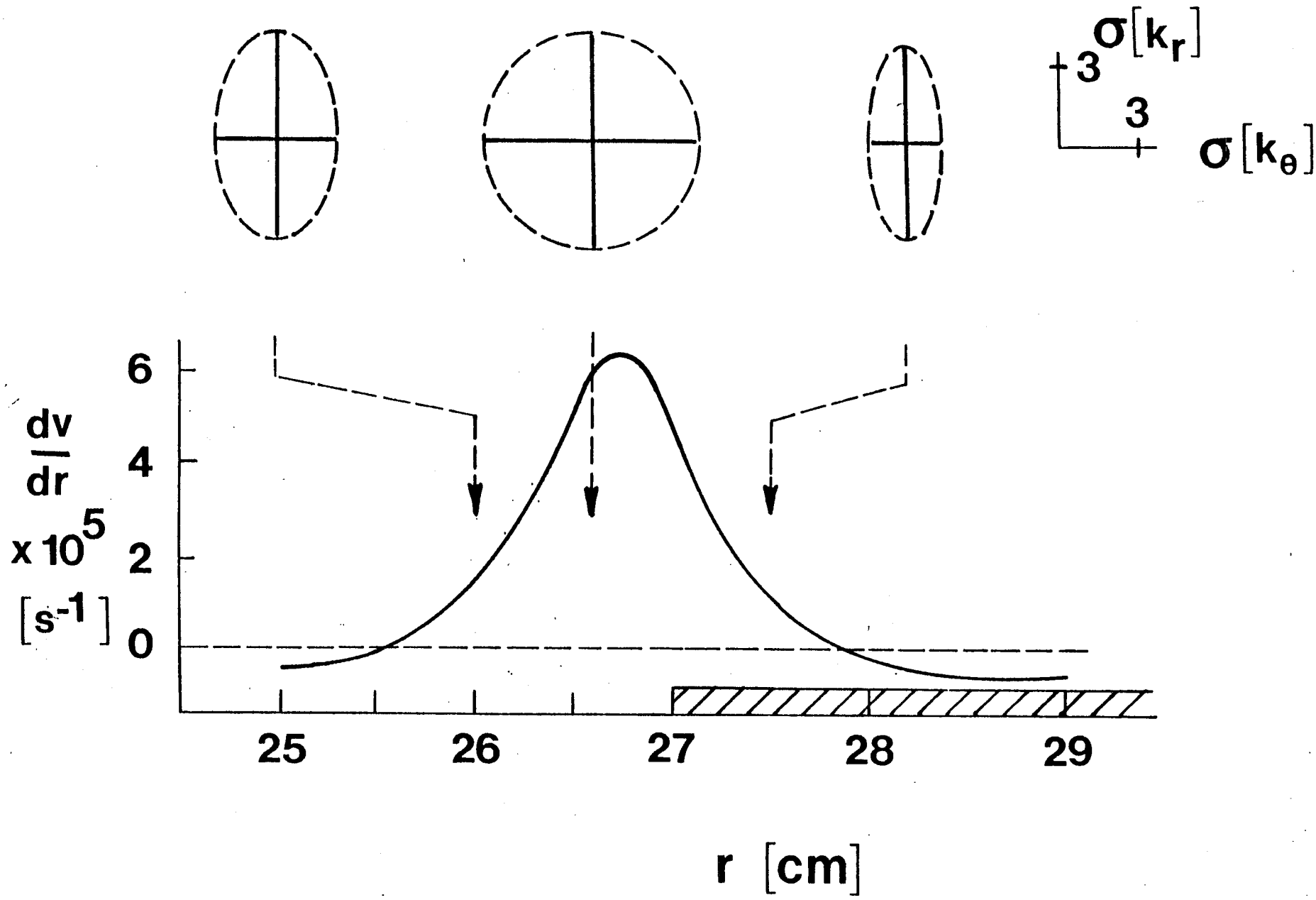

FIG. 1

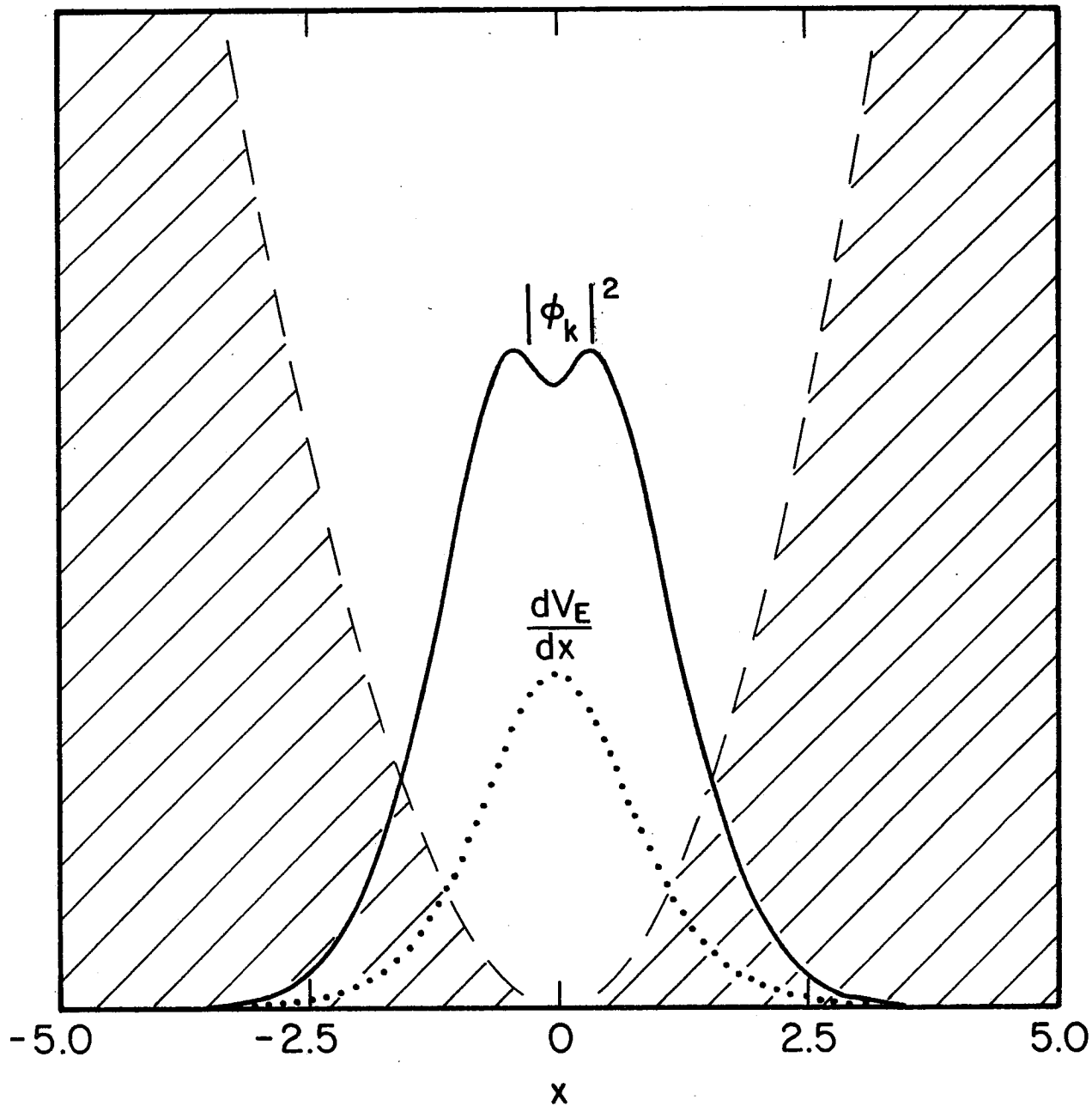

FIG. 2

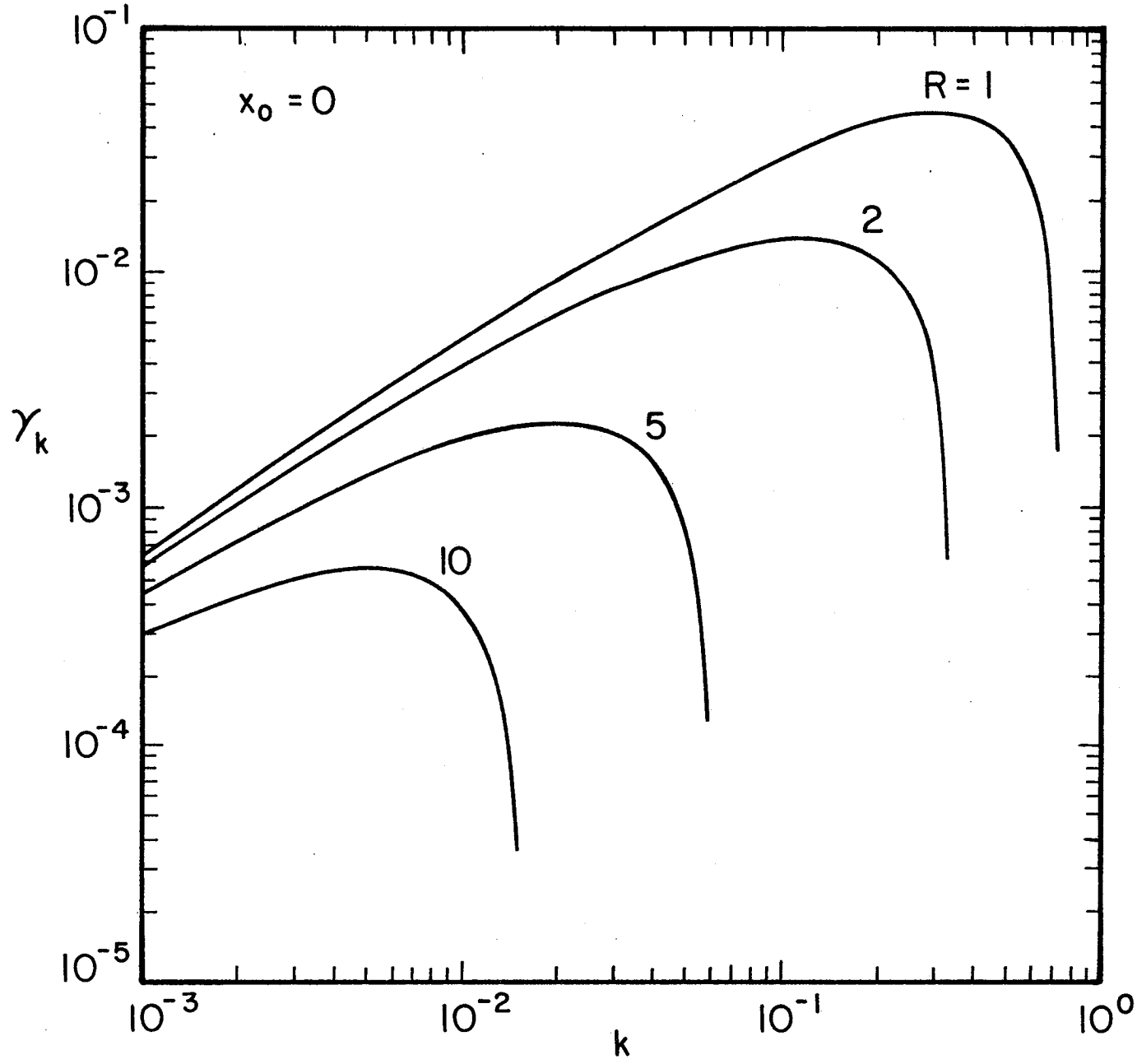

FIG. 3

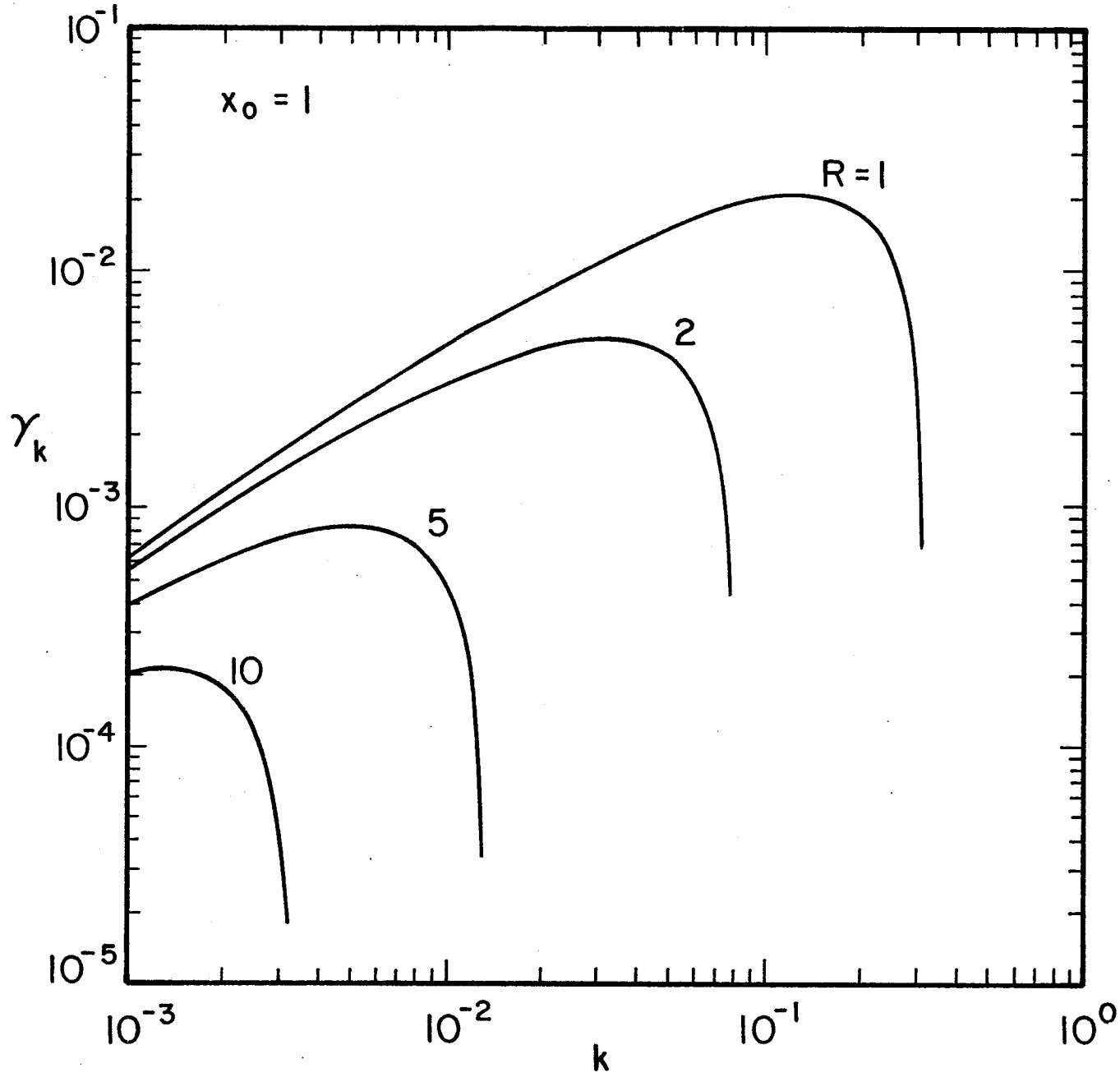

FIG. 4

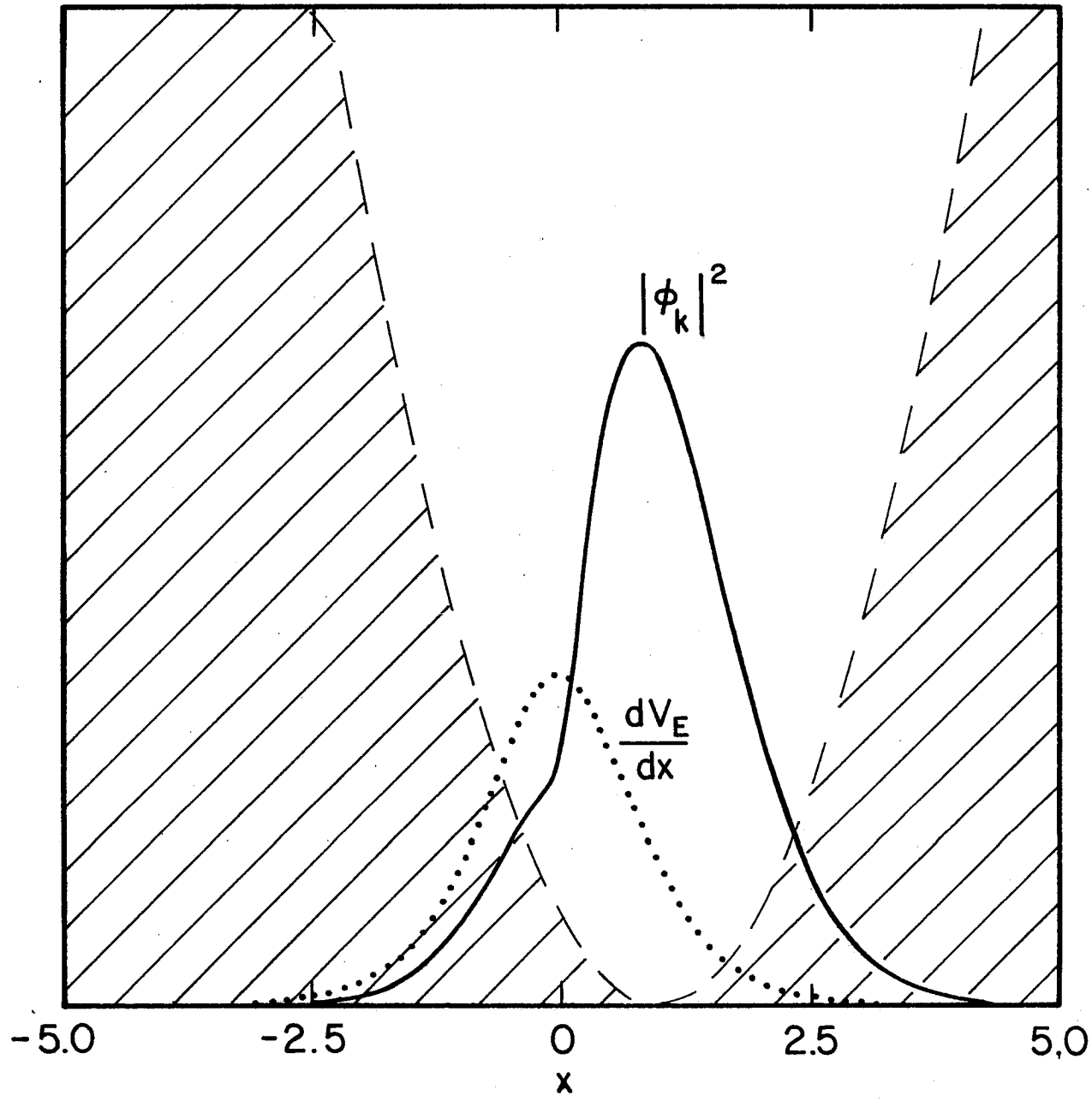

FIG. 5

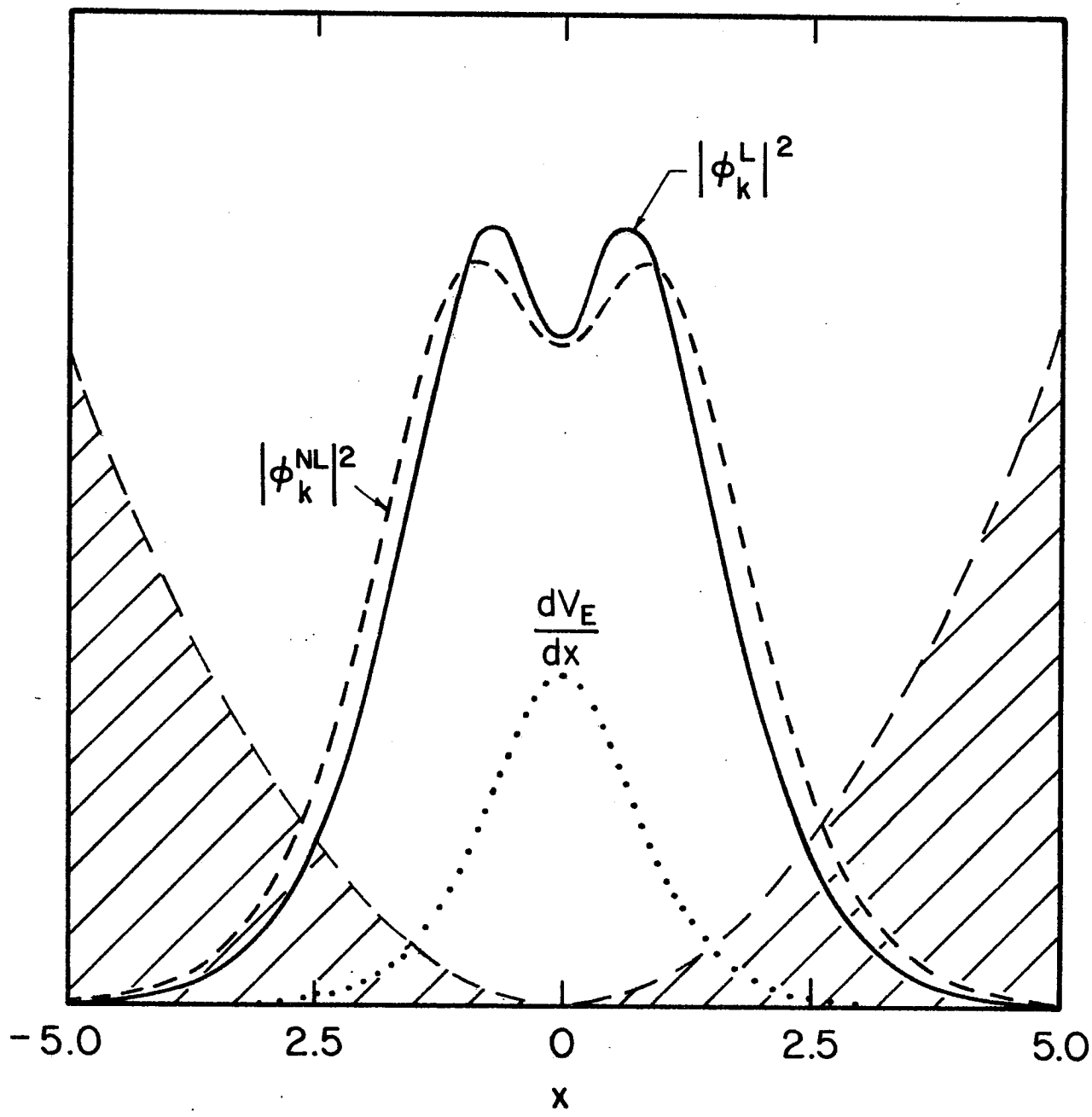

FIG. 6